AGU PUBLICATIONS

Geophysical Research Letters

RESEARCH LETTER

10.1002/2014GL061153

Key Points:
- The 2014 Rat Islands M_w 7.9 earthquake ruptured within the Pacific slab
- It is the largest intermediate depth earthquake in 100 years
- This category of event presents poorly recognized seismic hazard for some zones

Supporting Information:
- Readme
- Movie S1
- Figure S1
- Figure S2
- Figure S3
- Figure S4
- Figure S5
- Figure S6

Correspondence to:
T. Lay,
tlay@ucsc.edu

Citation:
Ye, L., T. Lay, and H. Kanamori (2014), The 23 June 2014 M_w 7.9 Rat Islands archipelago, Alaska, intermediate depth earthquake, *Geophys. Res. Lett.*, *41*, doi:10.1002/2014GL061153.

Received 7 JUL 2014
Accepted 6 SEP 2014
Accepted article online 11 SEP 2014

The 23 June 2014 M_w 7.9 Rat Islands archipelago, Alaska, intermediate depth earthquake

Lingling Ye[1], Thorne Lay[1], and Hiroo Kanamori[2]

[1]Department of Earth and Planetary Sciences, University of California, Santa Cruz, California, USA, [2]Seismological Laboratory, California Institute of Technology, Pasadena, California, USA

Abstract On 23 June 2014, the largest intermediate depth earthquake (M_w 7.9) of the last 100 years ruptured within the subducting Pacific plate about 100 km below the Rat Islands archipelago of the Western Aleutian Islands, Alaska. The unusual faulting orientation, strike = 206°, dip = 24°, and rake = −14°, is possibly related to curvature of the underthrust slab and high obliquity of the relative plate motions. The first ~15 s of the rupture generated relatively weak seismic waves, followed by strong energy release for the next 25 s. The seismic moment is 1.0×10^{21} Nm, and slip of up to ~10 m is concentrated within a 50 km × 50 km region. The radiated energy is 1.1 to 2.7×10^{16} J, assuming attenuation t^* of 0.4 to 0.7 s. This type of intraplate faulting can be very damaging for populated regions above subduction zones such as Japan, Taiwan, Chile, and Indonesia.

1. Introduction

Large subduction zone earthquakes usually involve thrust faulting at shallow depths offshore on the plate boundary megathrust fault, producing both shaking and tsunami hazards for nearby regions. Large intraplate earthquakes also occur in subduction zones, including normal faulting events near the outer trench slope; the largest known example being the great (M_S ~8.3+) 1933 Sanriku-oki earthquake [e.g., *Kanamori*, 1971]. The shaking and tsunami hazard of these near-trench events are now broadly recognized [e.g., *Lay et al.*, 2009, 2011], although it remains difficult to quantify. Less well recognized are the hazards presented by large intraslab earthquakes at depths of ~70 to 200 km, which places them between the coastline and volcanic arc. While not tsunamigenic, the relatively high stress drops commonly observed for intraplate events can result in strong ground shaking from these events. Recent examples include the 78 km deep 30 September 2009 M_w 7.6 Indonesia earthquake which struck near the city of Padang [e.g., *McCloskey et al.*, 2010], taking more than 1100 lives, and the 95 km deep 13 June 2005 M_w 7.8 Tarapaca, Chile earthquake [e.g., *Delouis and Legrand*, 2007]. Comparable size events at these depths are infrequent but have struck beneath Fiji, the Philippines, Hokkaido, Peru, the Solomon Islands, and Romania in the past 35 years; and the largest magnitude intermediate depth events of this type appear to be M ~8.1 events in 1903 beneath Kythira, Greece [*Papadopoulos and Vassilopoulou*, 2001] and in 1911 under the Ryukyu Islands [*Allen et al.*, 2009]. Large population centers such as Taipei, Taiwan, and Tokyo, Japan are exposed to risk from this type of intermediate depth faulting [e.g., *Kanamori et al.*, 2012]. Complex internal slab deformation is involved in such events, and the seismic hazard framework of these events is not clearly defined.

On 23 June 2014, the largest magnitude intermediate depth (70–300 km) earthquake to strike in 100 years ruptured within the subducting Pacific slab beneath the Rat Islands archipelago of the Western Aleutians, Alaska (Figure 1). The hypocenter (51.797°N, 178.760°E, 107.5 km deep, 20:53:09 UTC) (U.S. Geological Survey (USGS) National Earthquake Information Center (NEIC)): (http://earthquake.usgs.gov/regional/neic/) is downdip of the curving Aleutian trench in a region of highly oblique relative plate motion, with the Pacific plate underthrusting the North American plate at about 75 mm/yr [e.g., *DeMets et al.*, 2010]. Aftershocks spread northwestward from the hypocenter with depths spanning 90 to 140 km and about 50 km horizontal extent. Two of the largest early aftershocks are shallow strike-slip events, apparently being triggered events in the North American crust. While fortunately in a low-population region, this event is representative of the intermediate depth ruptures that can pose hazards in some subduction zones.

©2014. American Geophysical Union. All Rights Reserved.

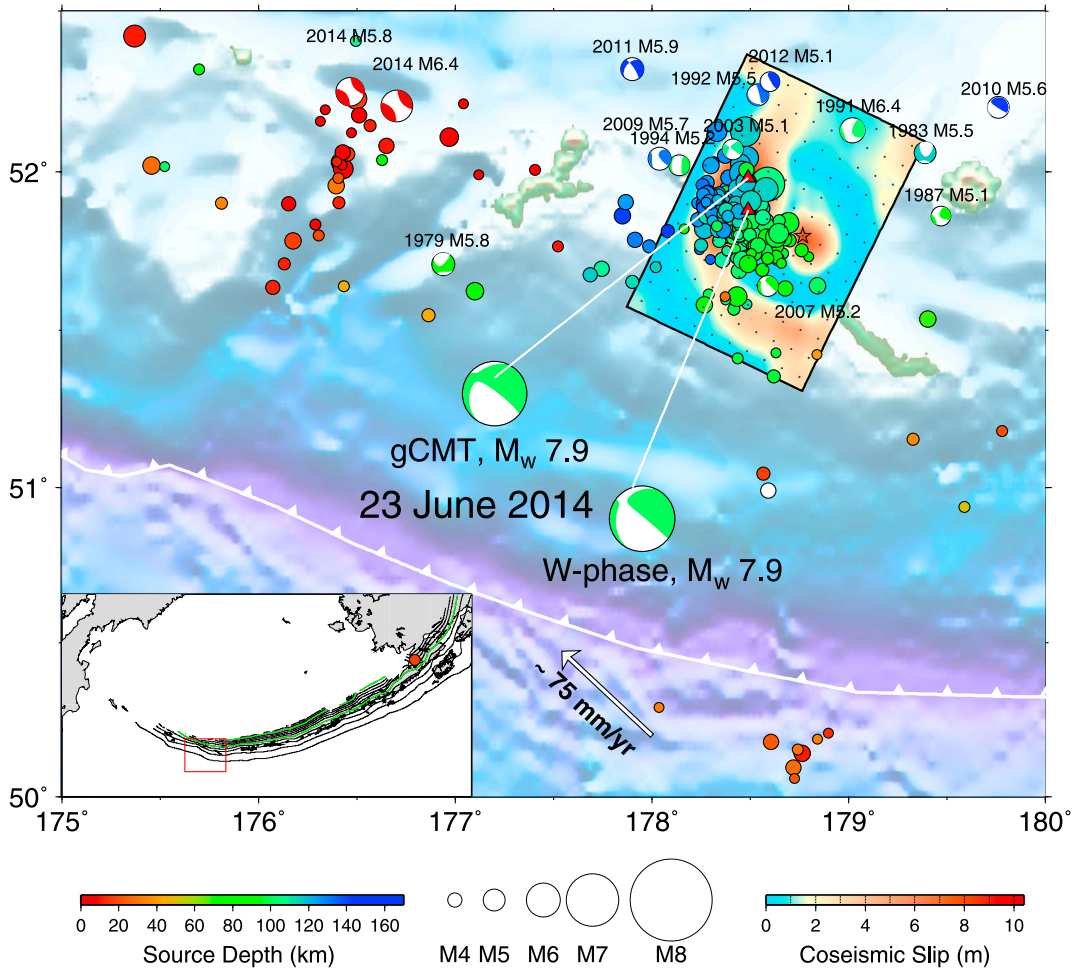

Figure 1. Map showing the rupture model and aftershocks in the first 2 months for the 23 June 2014 M_w 7.9 Rat Islands archipelago intermediate depth earthquake. The inset locates the source region in the western Aleutian Islands, Alaska, with the trench location and 100 km depth contours indicating the position of the underthrusting Pacific plate. The global centroid moment tensor (gCMT) and W-phase moment tensor solutions for the main shock are shown along with their associated centroid locations (red triangles) relative to the hypocenter from the USGS NEIC (star). Moment tensor solutions for all 70–200 km deep events in the gCMT catalog from 1976 to 2014 preceding the earthquake are shown with corresponding year and M_w labeled. Aftershocks with $M_w \geq 3$ are shown by circles, color coded with source depth and radius-scaled proportional to magnitude, including two shallow events with rapid gCMT solutions in the west. The preferred slip model is shown with total coseismic slip indicated by the color scale at bottom right. The barbed curve indicates the position of the Aleutian trench. The white arrow indicates the highly oblique motion of the Pacific plate relative to a fixed North America plate (model, MORVEL [*DeMets et al.,* 2010]).

2. Rupture Analysis

Point-source focal mechanisms for the 2014 Rat Islands earthquake obtained from long-period seismic wave methods give consistent, predominantly double-couple, faulting geometries. The global centroid moment tensor (GCMT) solution (http://www.globalcmt.org/CMTsearch.html) has major double-couple nodal planes with strike $\phi = 207°$, dip $\delta = 26°$, and rake $\lambda = -13°$ and $\phi = 308°$, $\delta = 84°$, and $\lambda = -115°$, a centroid depth of 100.8 km, a centroid time shift of 22.9 s, and a seismic moment $M_0 = 1.0 \times 10^{21}$ N m. We performed moment tensor inversions of 1–5 mHz passband W-phase signals [*Kanamori and Rivera*, 2008] using 132 ground motion recordings from 58 stations, obtaining a solution with best nodal planes with $\phi = 205.9°$, $\delta = 23.6°$, $\lambda = -14.1°$ and $\phi = 308.8°$, $\delta = 84.4°$, and $\lambda = -113.0°$, a centroid depth of 100.5 km, a centroid time shift of 22.9 s, and $M_0 = 1.0 \times 10^{21}$ N m. These solutions give M_w 7.9, and both have a null axis striking close to the relative plate motion direction (Figure 1), representing either subhorizontal or nearly vertical shearing of the slab.

©2014. American Geophysical Union. All Rights Reserved.

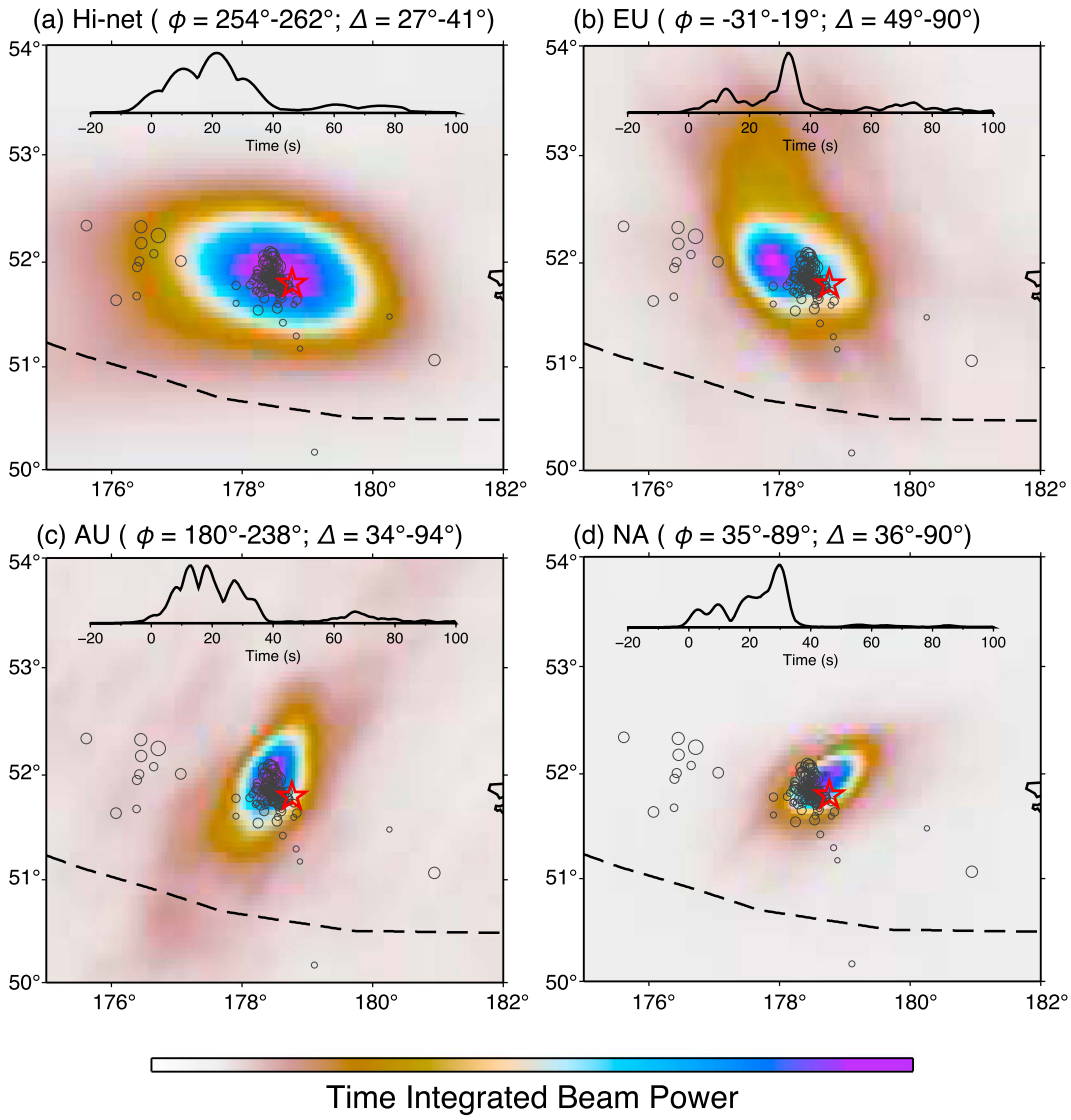

Figure 2. Imaged locations of coherent short-period seismic energy release from the 23 June 2014 M_w 7.9 Rat Islands archipelago earthquake obtained by backprojection of teleseismic *P* wave recordings in the period range of 0.5 to 2.0 s from large networks of (a) Hi-net stations in Japan, (b) broadband stations in Europe (EU), (c) broadband stations in Australia and South Pacific (AU), and (d) broadband stations in North America (NA). The time-integrated normalized beam power for each backprojection is shown with the color scale ranging from zero (white) to 1.0 (purple). The peak beam amplitudes as a function of time are shown at the top of each panel. The stations used in each backprojection are shown in maps in Figure S1 in the supporting information. The azimuthal (φ) and distance (Δ) ranges of the stations in each network are shown. Animations of the time-varying sequence for each backprojection are also provided in the supporting information.

Backprojections of teleseismic *P* wave recordings from large networks of stations in Japan (short-period Hi-net stations), Europe (EU), Australia and the South Pacific (AU), and North America (NA) were performed using the method of *Xu et al.* [2009]. The four networks all indicate 50 to 100 km westward rupture propagation over an interval of about 40 s, as shown by time-integrated maps of the coherent short-period energy release in the passband 0.5–2.0 s (Figure 2). The associated station configurations are shown in supporting information Figure S1, and animations of the time-varying backprojections are shown in Movie S1. The slightly west-northwestward distribution of energy release corresponds with the distribution of aftershocks in the first 10 days after the event. Array response artifacts smear the images slightly along the great-circle directions to the networks, and there is no direct resolution of depth extent of the rupture from this method. However, indications of modest north-south broadening of the rupture are apparent in the animations,

©2014. American Geophysical Union. All Rights Reserved.

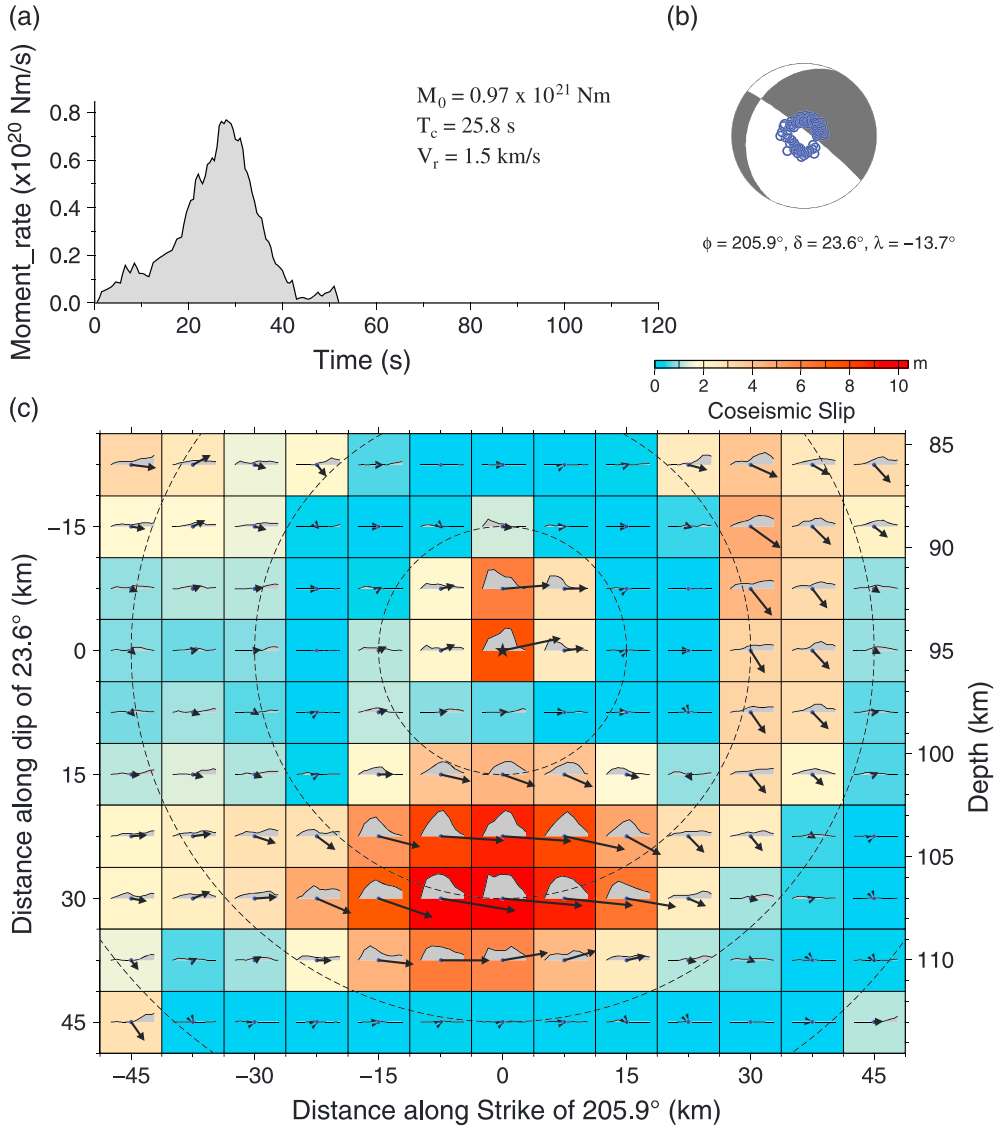

Figure 3. Rupture model for the preferred shallow-dipping rupture plane of the 23 June 2014 M_w 7.9 Rat Island archipelago earthquake obtained by linear waveform inversion of teleseismic *P* and *SH* ground displacements and ground velocities for the period band 1.1–200 s. Corresponding waveform fits are shown in Figure S2. (a) The moment rate function with the body wave inversion estimates of seismic moment, M_0, rupture centroid time T_c, and average rupture expansion velocity V_r. (b) The average fault geometry focal mechanism, with strike, ϕ, dip, δ, and rake, λ for the preferred fault plane. (c) Slip distribution on the model fault plane, which has 7.5 km grid spacing. The average slip for each subfault is color coded, and the vectors indicate the slip magnitude and direction of the hanging-wall plane relative to the footwall. The dashed circles are isochrones for the expanding rupture front in 10 s increments. The subfault source time functions are indicated by the polygons in each subfault, with the total rupture duration of each being 9 s. The star indicates the position of the hypocenter and corresponds to the star in Figure 1.

which slightly favor the shallow-dipping nodal plane. The limited spatial resolution does not tightly bound the rupture velocity, but all the images favor a modest horizontal extent of the rupture zone, which indicates a low apparent horizontal rupture expansion velocity of about ~1.5 km/s.

The point-source solutions and backprojections guided the development of a finite-fault rupture model inverted from broadband teleseismic *P* and *SH* wave ground motions, with the favored model being shown in Figures 1 and 3. Ground displacement and ground velocity signals from 63 *P* waves and 49 *SH* recordings were inverted. A 13 column by 10 row grid of subfaults with 7.5 km grid spacing was used in a linear least

©2014. American Geophysical Union. All Rights Reserved.

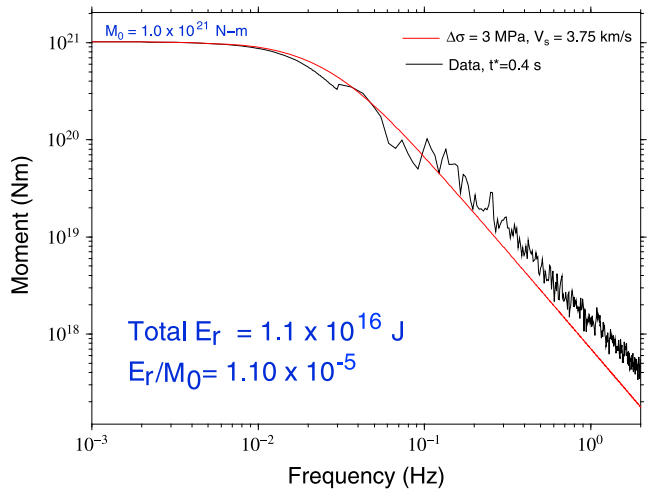

Figure 4. Average source spectrum for the 23 June 2014 Rat Islands archipelago M_w 7.9 intermediate depth earthquake. The spectrum of the moment rate function (Figure 3) is used for spectral amplitudes for frequencies less than 0.05 Hz, whereas averaged spectra from teleseismic *P* wave ground displacements, corrected for an average $t^* = 0.4$ s, are used for the higher-frequency spectrum. The radiated seismic energy, E_r, is estimated from the teleseismic *P* wave ground velocities and augmented for the proportion of energy in the average spectrum for frequencies below 0.05 Hz.

squares inversion with specified rupture expansion velocity [*Kikuchi and Kanamori*, 1991]. Each subfault was allowed to have variable rake, with the subfault source time function prescribed by eight overlapping triangles with 1 s rise times, giving subfault durations of up to 9 s. The hypocentral depth was designated as 95 km. The strike and dip of the fault plane were taken from the shallow-dipping nodal plane of the W-phase solution. Inversions were performed for a wide range of rupture velocities, grid dimensions, and subfault durations. Corresponding suites of models were computed for the steeply dipping nodal plane of the W-phase solution. We sought models that gave seismic moments consistent with the long-period moment tensor values and centroid time shifts within a few seconds of the point-source solutions.

The shallow-dipping fault plane with $\phi = 205.9°$ and $\delta = 23.6°$ toward the northwest provides better matches to *P* waveforms at azimuths from 300° to 340° (Figure S2) than does the steeply dipping fault plane solution (Figures S3 and S4). However, the overall waveform mismatch is comparable between the models, and some signals are better fit using the steeply dipping fault plane (notably for *P* arrivals at lapse times of 30 s for stations with azimuths around 135°–180°), so our preference for the shallow-dipping plane is mild. The USGS-NEIC finite-fault model solution also adopts the shallow-dipping plane. Comparison of the catalog aftershock locations with the two possible fault planes does not provide compelling evidence to favor either plane (Figure S5), but the horizontal spread of the aftershocks and the backprojection images is more straightforward to reconcile with the horizontal plane. We cannot preclude rupture over a set of horizontally offset vertical faults. Aftershocks may also occur on separate structures, and this is clearly the case for shallow events in the upper plate located to the west of the epicenter (Figure 1).

The moment rate function has relatively low level for about the first 15 s of the rupture, and the waveforms show small short-period pulses during this interval that are hard to match in the finite-fault inversion. This interval is followed by a large triangular pulse with about 25 s duration (Figure 3). W-phase and body wave inversions of short-time windows of the first 25 s of the teleseismic signals do not resolve significantly different faulting geometry of the early radiation. Typical of teleseismic inversions, particularly for intraplate ruptures, the data have limited resolution of rupture velocity. However, using 1.5 km/s as suggested by the backprojections provides a solution that is slightly favored in terms of waveform fit and places the primary slip regions in the vicinity of the aftershock distribution (Figure 1). The rupture velocity and subfault source time function parameterization have significant trade-offs in controlling the spatial distribution of slip. The slip function for this model shows about 6 m of slip near the hypocenter followed by a 30 km × 30 km patch of large slip (up to 10.3 m) centered about 25 km downdip (toward the northwest) (Figure 3). Similar northwestward offset of the main pulse is found for the steeply dipping fault plane (Figure S3). The seismic moment is 1.0×10^{21} N m, and the centroid time shift is 25.8 s, with the average depth of the slip distribution being 101 km, so the model in Figure 3 is compatible with long-period point-source constraints. Trimming off subfaults that have less than 15% of the peak subfault moment, the rupture area is found to be 3487.5 km^2, and the average slip is 3.9 m. Assuming a circular rupture area, the static stress drop is 11.8 MPa. These estimates have substantial uncertainties corresponding to the limited spatial resolution of the teleseismic inversion.

©2014. American Geophysical Union. All Rights Reserved.

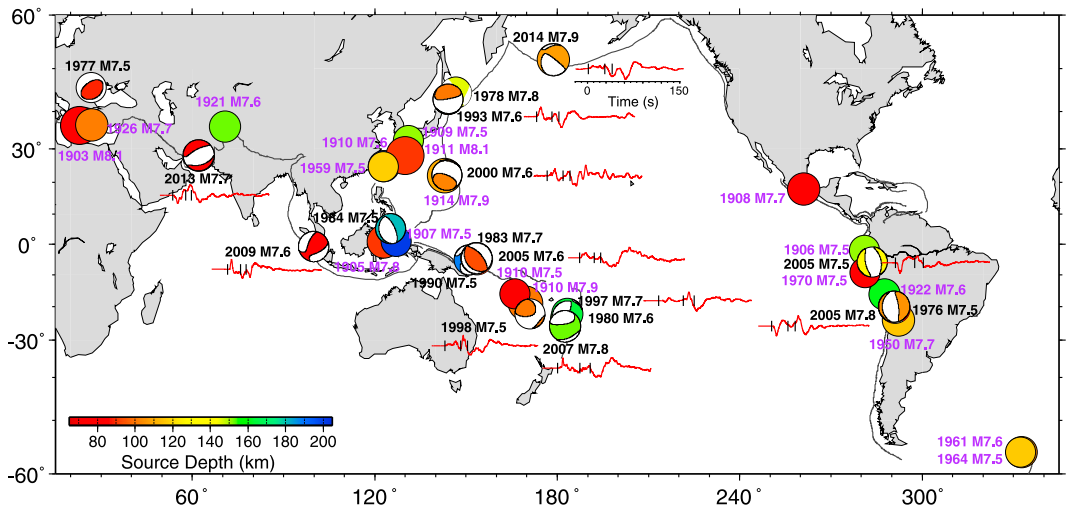

Figure 5. Map showing the global distribution of all 37 earthquakes in the depth range 70 to 200 km between 1900 and 2014 with $M_w \geq 7.5+$ from the PAGER-CAT [*Allen et al.*, 2009], with events since 1976 displayed as the GCMT moment tensor. For the recent large events, a broadband *P* wave ground displacement is shown with tick marks indicating the *P*, *pP*, and *sP* arrival times (all have the same time scale with 20 s leader ahead of the *P* arrival and 150 s of signal after that). Figure S6 identifies the specific stations shown for each event. Some events may actually be shallower events with over-estimated depth in the catalog, and some events actually in this depth range may be missed because the catalog depths are incorrectly estimated as less than 70 km.

The average source spectrum is shown in Figure 4, along with the measured radiated energy, E_r. The source spectrum is obtained from the spectrum of the moment rate function for frequencies less than 0.05 Hz, and from the stack average of broadband *P* wave displacement spectra, corrected for radiation pattern and an attenuation operator with $t^* = 0.4$ s, for higher frequencies. The specific choice of t^* is not well resolved. The intermediate depth of the event and the presence of the steeply dipping subducting slab traversed by the down-going signals below the source motivate a relatively low t^*. This source spectrum is slightly enriched in high-frequency spectral levels relative to a reference ω-squared source spectrum with a stress parameter of 3 MPa. For the frequency band from 0.0 to 2.0 Hz the total radiated energy $E_R = 1.1 \times 10^{16}$ J, for a $t^* = 0.4$ s. This estimate is based on the methodology of *Venkataraman and Kanamori* [2004] applied to teleseismic *P* wave ground velocities, augmented by the relative proportion of energy in the spectrum for frequencies less than 0.05 Hz [e.g., *Ye et al.*, 2013]. The corresponding seismic moment-scaled energy ratio is $E_R/M_0 = 1.1 \times 10^{-5}$. Use of a higher $t^* = 0.7$ s gives $E_R = 2.7 \times 10^{16}$ J for the same passband.

3. Discussion and Conclusions

The 23 June 2014 M_w 7.9 Rat Islands archipelago earthquake ruptured within the subducting Pacific plate downdip from the megathrust fault that produced the great 4 February 1965 M_w 8.7 Rat Island earthquake [e.g., *Wu and Kanamori*, 1973; *Beck and Christensen*, 1991]. That event induced a large M_w 7.6 trench slope normal faulting aftershock on 30 March 1965 [*Abe*, 1972], as commonly observed seaward of great interplate ruptures [e.g., *Lay et al.*, 1989; *Craig et al.*, 2014]. Such intraplate faulting may provide hydrated zones that can be reactivated as the slab sinks to intermediate depths and undergoes dehydration reactions that release fluids and reduce confining stresses on the fault zone. This general scenario is commonly invoked to account for intermediate depth earthquakes as fluid-assisted dehydration embrittlement faulting, although self-localizing thermal shear runaway mechanisms are also considered viable [*Prieto et al.*, 2013]. Even if correct in general, reactivation of prior fault systems does not provide a simple strain accumulation and release context like that for the relative plate motions driving megathrust faulting to provide guidance on the frequency of large intermediate depth events. The best approach that we have is to characterize the attributes of such events based on the limited number of recorded examples and to recognize their general potential in earthquake hazard assessments.

©2014. American Geophysical Union. All Rights Reserved.

The faulting orientation for the 2014 Rat Islands event is not easily related to geometry of shallow plate bending faults, with the deeper slab either displacing northeastward on the favored shallow-dipping plane or almost vertically downward on the steeply dipping plane. Given the increasing obliquity of the relative plate motions along the curving Aleutian trench, contortion of the subducted Pacific plate is expected to affect the intraplate stresses in the slab beneath the Rat Islands archipelago [e.g., *Creager and Boyd*, 1991; *Ruppert et al.*, 2007], but the faulting orientation may be influenced by inherited shallow intraplate fault zone structure.

The distribution of large earthquakes at depths from 70 to 200 km with $M_w \geq 7.5$ from the seismological record is shown in Figure 5. Epicenters of events dating back to 1900 are shown by circles, and GCMT focal mechanisms are shown for the events since 1976. Comparisons of teleseismic *P* waveforms from several of the larger recent events are included, demonstrating the overall similarity of the 2014 event signals to events in other regions. The map indicates the global extent of this class of intraslab earthquakes relative to population centers. Slabs with varying thermal structures, convergence rates, and geometries experience large intermediate depth events, and detailed work is required to evaluate whether there are any tectonic controls on their occurrence that could guide hazard assessments. Each region likely has unique tectonic stresses and inherited faulting geometries from shallower plate bending, making it difficult to infer recurrence and total distribution of such events from the short seismological record along with the lack of geologic record; but at a minimum, recognition of this class of infrequent large ruptures should be incorporated into seismic hazard assessments in populated subduction zone environments.

Acknowledgments
The IRIS DMS (http://www.iris.edu/hq/) and Orpheus (http://www.orfeus-eu.org) data centers were used to access the seismic data from Global Seismic Network and Federation of Digital Seismic Network stations, and the Hi-net data center (http://www.hinet.bosai.go.jp/about_data/?LANG=en) of NIED was used to access Hi-net recordings. This work made use of GMT and SAC software. K. Koper provided access to and training with his backprojection software. We thank two anonymous reviewers for their helpful comments. This work was supported by NSF grant EAR1245717 (T.L.).

The Editor thanks two anonymous reviewers for their assistance in reviewing this paper.

References

Abe, K. (1972), Lithospheric normal faulting beneath the Aleutian trench, *Phys. Earth Planet. Inter.*, *5*, 190–198.

Allen, T. I., K. D. Marano, P. S. Earle, and D. J. Wald (2009), PAGER-CAT: A composite earthquake catalog for calibrating global fatality models, *Seismol. Res. Lett.*, *80*, 57–62, doi:10.1785/gssrl.80.1.57.

Beck, S. L., and D. H. Christensen (1991), Rupture process of the February 4, 1965, Rat Islands earthquake, *J. Geophys. Res.*, *96*, 2205–2221, doi:10.1029/90JB02092.

Craig, T. J., A. Copley, and J. Jackson (2014), A reassessment of outer-rise seismicity and its implications for the mechanics of oceanic lithosphere, *Geophys. J. Int.*, *197*, 63–89, doi:10.1093/gji/ggu013.

Creager, K. C., and T. M. Boyd (1991), The geometry of Aleutian subduction: Three-dimensional kinematic flow model, *J. Geophys. Res.*, *96*, 2293–2307, doi:10.1029/90JB01918.

Delouis, B., and D. Legrand (2007), M_w 7.8 Tarapaca intermediate depth earthquake of 13 June 2005 (northern Chile): Fault plane identification and slip distribution by waveform inversion, *Geophys. Res. Lett.*, *34*, L01304, doi:10.1029/2006GL028193.

DeMets, C., R. G. Gordon, and D. F. Argus (2010), Geologically current plate motions, *Geophys. J. Int.*, *181*, 1–80, doi:10.1111/j.1365-246X.2009.04491.x.

Kanamori, H. (1971), Seismological evidence for a lithospheric normal faulting—The Sanriku earthquake of 1933, *Phys. Earth Planet. Inter.*, *4*, 289–300.

Kanamori, H., and L. Rivera (2008), Source inversion of W phase: Speeding up seismic tsunami warning, *Geophys. J. Int.*, *175*, 222–238.

Kanamori, H., W. H. K. Lee, and K.-F. Ma (2012), The 1909 Taipei earthquake—Implications for seismic hazard in Taipei, *Geophys. J. Int.*, *191*, 126–146, doi:10.1111/j.1365-246X.2012.05589.x.

Kikuchi, M., and H. Kanamori (1991), Inversion of complex body waves—III, *Bull. Seismol. Soc. Am.*, *81*(6), 2335–2350.

Lay, T., L. Astiz, H. Kanamori, and D. H. Christensen (1989), Temporal variation of large intraplate earthquakes in coupled subduction zones, *Phys. Earth Planet. Inter.*, *54*, 258–312.

Lay, T., H. Kanamori, C. J. Ammon, A. R. Hutko, K. Furlong, and L. Rivera (2009), The 2006-2007 Kuril Islands great earthquake sequence, *J. Geophys. Res.*, *114*, B113208, doi:10.1029/2008JB006280.

Lay, T., C. J. Ammon, H. Kanamori, M. J. Kim, and L. Xue (2011), Outer trench-slope faulting and the 2011 M_w 9.0 off the Pacific coast of Tohoku earthquake, *Earth Planets Space*, *63*, 713–718, doi:10.5047/eps.2011.05.006.

McCloskey, J., D. Lange, F. Tilmann, S. S. Nalbant, A. F. Bell, D. H. Natawidjaja, and A. Rietbrok (2010), The September 2009 Padang earthquake, *Nat. Geosci.*, *3*, 70–71, doi:10.1038/ngeo753.

Papadopoulos, G. A., and A. Vassilopoulou (2001), Historical and archeological evidence of earthquakes and tsunamis felt in the Kythira strait, Greece, in *Tsunami Research at the End of a Critical Decade*, edited by G. T. Hebenstreit, pp. 119–138, Springer, Berlin, Heidelberg, New York.

Prieto, G. A., M. Florez, S. A. Barrett, G. C. Beroza, P. Pedraza, J. F. Blanco, and E. Poveda (2013), Seismic evidence for thermal runaway during intermediate-depth earthquake rupture, *Geophys. Res. Lett.*, *40*, 6064–6068, doi:10.1002/2013GL058109.

Ruppert, N. A., J. M. Lees, and N. P. Kozyreva (2007), Seismicity, earthquakes and structure along the Alaska-Aleutian and Kamchatka-Kurile subduction zones: A review, in *Volcanism and Subduction: The Kamchatka Region*, *Geophys. Monogr. Ser.*, vol. 172, edited by J. Eichelberger et al., pp. 129–144, AGU, Washington, D. C.

Venkataraman, A., and H. Kanamori (2004), Observational constraints on the fracture energy of subduction zone earthquakes, *J. Geophys. Res.*, *109*, B05302, doi:10.1029/2003JB002549.

Wu, F. T., and H. Kanamori (1973), Source mechanism of February 4, 1965, Rat Island earthquake, *J. Geophys. Res.*, *78*, 6082–6092, doi:10.1029/JB078i026p06082.

Xu, Y., K. D. Koper, O. Sufri, L. Zhu, and A. R. Hutko (2009), Rupture imaging of the M_w 7.9 12 May 2008 Wenchuan earthquake from back projection of teleseismic P waves, *Geochem. Geophys. Geosyst.*, *10*, Q04006, doi:10.1029/2008GC002335.

Ye, L., T. Lay, H. Kanamori, and K. D. Koper (2013), Energy release of the 2013 M_w 8.3 Sea of Okhotsk earthquake and deep slab stress heterogeneity, *Science*, *341*, 1380–1384.

©2014. American Geophysical Union. All Rights Reserved.

Supporting Material for Paper 2014GLXXXXXX

The 23 June 2014 Rat Islands archipelago, Alaska Mw 7.9 intermediate depth earthquake

Lingling Ye(1), Thorne Lay(1,*), and Hiroo Kanamori(2)

(1) Department of Earth and Planetary Sciences, University of California Santa Cruz, Santa Cruz, CA 95064, USA.
(2) Seismological Laboratory, California Institute of Technology, Pasadena, CA 91125 USA.
(*) Corresponding author: Thorne Lay (tlay@ucsc.edu; 831-459-3164)

Introduction

Auxiliary materials comprise 6 figures and one QuickTime animation.

Figure S1. Locations of stations (circles) recording P waves used in backprojections for four different networks in (a) Japan (Hi-net), (b) Europe, (c) Australia and South Pacific, and (d) North America. The average correlation coefficients from multi-station correlations are shown by the color scale.

Figure S2. Comparison of observed (black) and synthetic (red) P and SH ground motions for the preferred rupture model shown in Figure 3. For each station, the azimuth from the source (φ) and epicentral distance (Δ) are indicated, along with the peak-to-peak ground motion in microns (blue numbers). The observed signal (black traces) amplitudes are normalized. The red curves are true relative amplitude synthetic waveforms. For each station the first trace is ground displacement and the second trace is ground velocity.

Figure S3. Rupture model for the steeply dipping plane for the 23 June 2014 Mw 7.9 Rat Island archipelago earthquake obtained by linear waveform inversion of teleseismic P and SH ground displacements and ground velocities for the period band 1.1-200 s. Corresponding waveform fits are shown in Figure S4. (a) The moment rate function with the body wave inversion estimates of seismic moment, M0, rupture centroid time Tc, and average rupture expansion velocity Vr. (b) The average fault geometry focal mechanism, with strike, φ, dip, δ, and rake, λ for the preferred fault plane. (c) Slip distribution on the model fault plane, which has 7.5 km grid spacing. The average slip for each subfault is color-coded and the vectors indicate the slip magnitude and direction of the hanging-wall plane relative to the foot-wall. The dashed circles are isochrones for the expanding rupture front in 10 s increments. The subfault source durations are indicated by the polygons in each subfault, with the total rupture duration of each being 9 s. The star indicates the position of the hypocenter, and corresponds to the star in Figure 1.

Figure S4. Comparison of observed (black) and synthetic (red) P and SH ground motions for the steeply-dipping fault plane rupture model shown in Figure S3. For each station, the azimuth from the source (φ) and epicentral distance (Δ) is indicated, along with the peak-to-peak ground motion in microns (blue numbers). The observed signal (black traces) amplitudes are normalized. The red curves are true relative amplitude synthetic waveforms. For each station the first trace is ground displacement and the second trace is ground velocity.

Figure S5. All aftershock locations from the USGS-NEIC are viewed in (a) map view with bathymetry and Aleutian trench (barbed line) shown, (b) vertical cross-section A-A' along an azimuth of 17° through the mainshock hypocenter, which is perpendicular to the local strike of the Aleutian trench with the red triangle indicating the trench position and the dashed cyan lines indicating the possible slab dipping angles, (c) vertical cross-section

B-B’ along an azimuth of 295.7° in the plunge direction of the shallow-dipping nodal plane, and (d) vertical cross-section C-C’ along an azimuths of 84.4° in the plunge direction of the steeply-dipping nodal plane. Earthquake hypocenters are shown by circles, color-coded with source depth and radius-scaled proportional to magnitude, as in Figure 1. The spread of aftershock locations does not allow unambiguous preference for a fault-plane, but in either case the source region appears to be spatially concentrated over a 50 km x 50 km extent.

Figure S6. Details about the seismograms shown for recent large intermediate depth earthquakes from 1993 to 2014 in Figure 5. For each event, a representative teleseismic P wave ground displacement recording from 64° to 79° is shown with a 20 s leader and 150 s of motion. Data are filtered in the passband 0.005 to 4.0 Hz. The waveforms are aligned on the P arrival, with the predicted arrival time of pP indicated by green tick marks and the sP arrival time indicated by blue tick marks. The amplitudes are normalized by the peak amplitude of each recording. The event location, year, Julian day, and station name are indicated, with the station azimuth (φ) and epicentral distance (Δ) and the PAGER-cat source depth (h) indicated.

Animation S1. QuickTime MOV file with H264 compression of back-projections for the 0.5-2.0 Hz P waves signals recorded at European (EU), North American (NA), Japanese (Hi-net), and Australia/South Pacific (AU) networks. The signal power at each time instant is plotted over the source region grid, with purple indicating maximum coherent power.

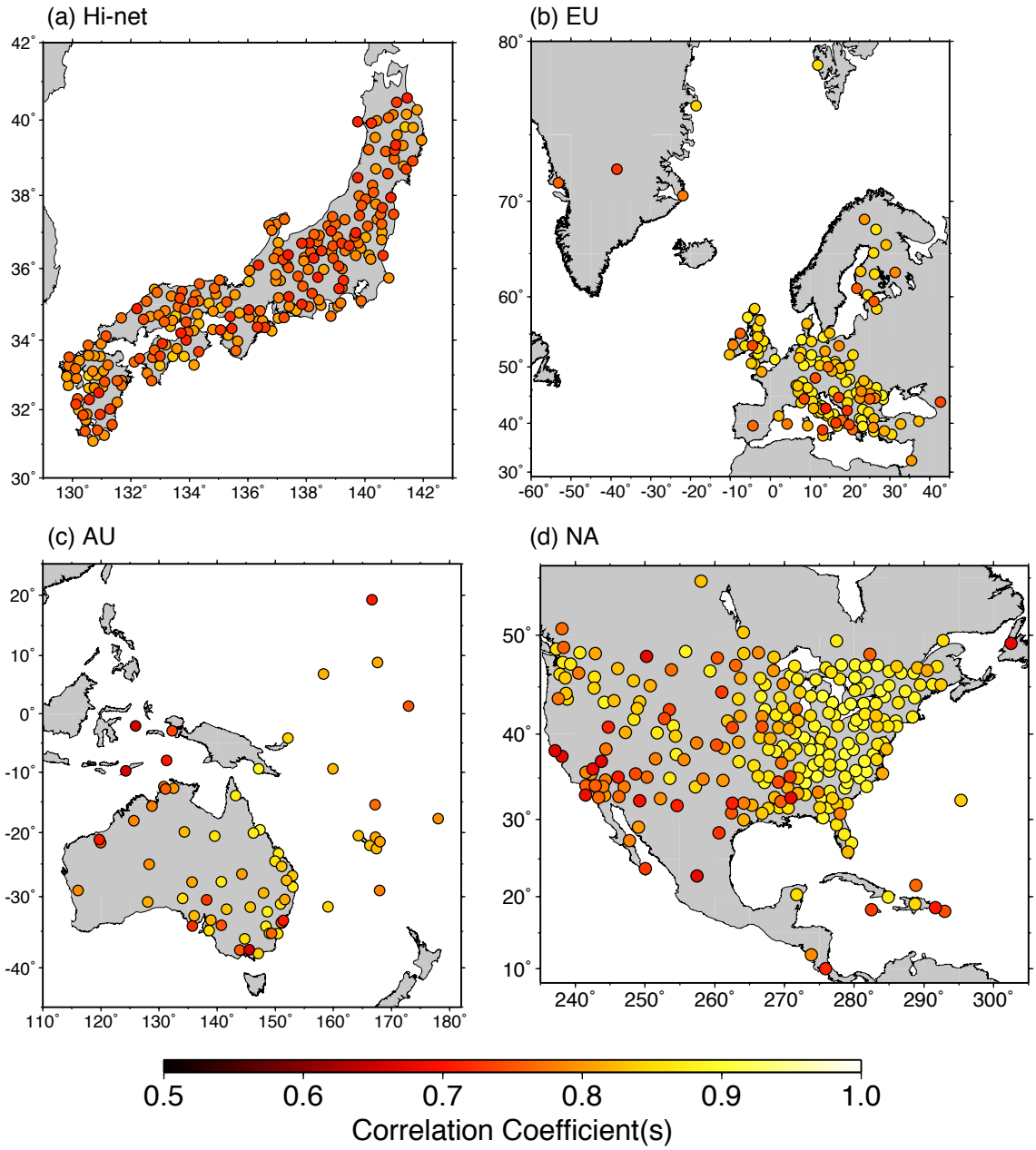
(a) Hi-net
42°
40°
38°
36°
34°
32°
30°
130°
132°
134°
136°
138°
140°
142°
(b) EU
80°
70°
60°
50°
40°
30°
-60°
-50°
-40°
-30°
-20°
-10°
0°
10°
20°
30°
40°
(c) AU
20°
10°
0°
-10°
-20°
-30°
-40°
110°
120°
130°
140°
150°
160°
170°
180°
(d) NA
50°
40°
30°
20°
10°
240°
250°
260°
270°
280°
290°
300°
0.5
0.6
0.7
0.8
0.9
1.0
Correlation Coefficient(s)

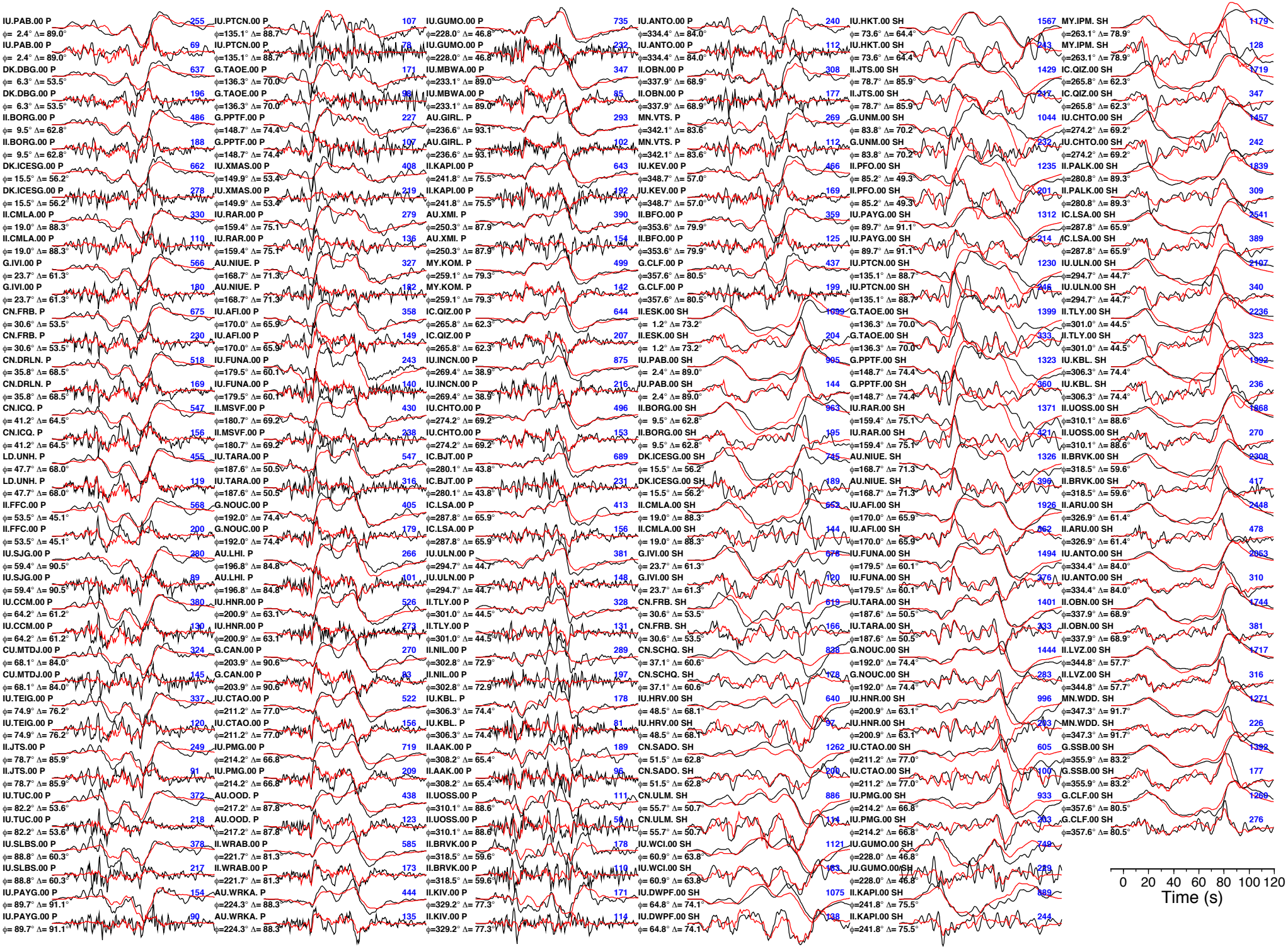
IU.PAB.00 P
ϕ= 2.4° Δ= 89.0°
IU.PAB.00 P
ϕ= 2.4° Δ= 89.0°
DK.DBG.00 P
ϕ= 6.3° Δ= 53.5°
DK.DBG.00 P
ϕ= 6.3° Δ= 53.5°
II.BORG.00 P
ϕ= 9.5° Δ= 62.8°
II.BORG.00 P
ϕ= 9.5° Δ= 62.8°
DK.ICESG.00 P
ϕ= 15.5° Δ= 56.2°
DK.ICESG.00 P
ϕ= 15.5° Δ= 56.2°
II.CMLA.00 P
ϕ= 19.0° Δ= 88.3°
II.CMLA.00 P
ϕ= 19.0° Δ= 88.3°
G.IVI.00 P
ϕ= 23.7° Δ= 61.3°
G.IVI.00 P
ϕ= 23.7° Δ= 61.3°
CN.FRB. P
ϕ= 30.6° Δ= 53.5°
CN.FRB. P
ϕ= 30.6° Δ= 53.5°
CN.DRLN. P
ϕ= 35.8° Δ= 68.5°
CN.DRLN. P
ϕ= 35.8° Δ= 68.5°
CN.ICQ. P
ϕ= 41.2° Δ= 64.5°
CN.ICQ. P
ϕ= 41.2° Δ= 64.5°
LD.UNH. P
ϕ= 47.7° Δ= 68.0°
LD.UNH. P
ϕ= 47.7° Δ= 68.0°
II.FFC.00 P
ϕ= 53.5° Δ= 45.1°
II.FFC.00 P
ϕ= 53.5° Δ= 45.1°
IU.SJG.00 P
ϕ= 59.4° Δ= 90.5°
IU.SJG.00 P
ϕ= 59.4° Δ= 90.5°
IU.CCM.00 P
ϕ= 64.2° Δ= 61.2°
IU.CCM.00 P
ϕ= 64.2° Δ= 61.2°
CU.MTDJ.00 P
ϕ= 68.1° Δ= 84.0°
CU.MTDJ.00 P
ϕ= 68.1° Δ= 84.0°
IU.TEIG.00 P
ϕ= 74.9° Δ= 76.2°
IU.TEIG.00 P
ϕ= 74.9° Δ= 76.2°
II.JTS.00 P
ϕ= 78.7° Δ= 85.9°
II.JTS.00 P
ϕ= 78.7° Δ= 85.9°
IU.TUC.00 P
ϕ= 82.2° Δ= 53.6°
IU.TUC.00 P
ϕ= 82.2° Δ= 53.6°
IU.SLBS.00 P
ϕ= 88.8° Δ= 60.3°
IU.SLBS.00 P
ϕ= 88.8° Δ= 60.3°
IU.PAYG.00 P
ϕ= 89.7° Δ= 91.1°
IU.PAYG.00 P
ϕ= 89.7° Δ= 91.1°
255 IU.PTCN.00 P
ϕ=135.1° Δ= 88.7°
69 IU.PTCN.00 P
ϕ=135.1° Δ= 88.7°
637 G.TAOE.00 P
ϕ=136.3° Δ= 70.0°
196 G.TAOE.00 P
ϕ=136.3° Δ= 70.0°
486 G.PPTF.00 P
ϕ=148.7° Δ= 74.4°
188 G.PPTF.00 P
ϕ=148.7° Δ= 74.4°
662 IU.XMAS.00 P
ϕ=149.9° Δ= 53.4°
278 IU.XMAS.00 P
ϕ=149.9° Δ= 53.4°
330 IU.RAR.00 P
ϕ=159.4° Δ= 75.1°
110 IU.RAR.00 P
ϕ=159.4° Δ= 75.1°
566 AU.NIUE. P
ϕ=168.7° Δ= 71.3°
180 AU.NIUE. P
ϕ=168.7° Δ= 71.3°
675 IU.AFI.00 P
ϕ=170.0° Δ= 65.9°
230 IU.AFI.00 P
ϕ=170.0° Δ= 65.9°
518 IU.FUNA.00 P
ϕ=179.5° Δ= 60.1°
169 IU.FUNA.00 P
ϕ=179.5° Δ= 60.1°
547 II.MSVF.00 P
ϕ=180.7° Δ= 69.2°
156 II.MSVF.00 P
ϕ=180.7° Δ= 69.2°
455 IU.TARA.00 P
ϕ=187.6° Δ= 50.5°
119 IU.TARA.00 P
ϕ=187.6° Δ= 50.5°
568 G.NOUC.00 P
ϕ=192.0° Δ= 74.4°
200 G.NOUC.00 P
ϕ=192.0° Δ= 74.4°
280 AU.LHI. P
ϕ=196.8° Δ= 84.8°
89 AU.LHI. P
ϕ=196.8° Δ= 84.8°
380 IU.HNR.00 P
ϕ=200.9° Δ= 63.1°
130 IU.HNR.00 P
ϕ=200.9° Δ= 63.1°
324 G.CAN.00 P
ϕ=203.9° Δ= 90.6°
145 G.CAN.00 P
ϕ=203.9° Δ= 90.6°
337 IU.CTAO.00 P
ϕ=211.2° Δ= 77.0°
120 IU.CTAO.00 P
ϕ=211.2° Δ= 77.0°
249 IU.PMG.00 P
ϕ=214.2° Δ= 66.8°
91 IU.PMG.00 P
ϕ=214.2° Δ= 66.8°
372 AU.OOD. P
ϕ=217.2° Δ= 87.8°
218 AU.OOD. P
ϕ=217.2° Δ= 87.8°
378 II.WRAB.00 P
ϕ=221.7° Δ= 81.3°
217 II.WRAB.00 P
ϕ=221.7° Δ= 81.3°
154 AU.WRKA. P
ϕ=224.3° Δ= 88.3°
90 AU.WRKA. P
ϕ=224.3° Δ= 88.3°
107 IU.GUMO.00 P
ϕ=228.0° Δ= 46.8°
78 IU.GUMO.00 P
ϕ=228.0° Δ= 46.8°
171 IU.MBWA.00 P
ϕ=233.1° Δ= 89.0°
98 IU.MBWA.00 P
ϕ=233.1° Δ= 89.0°
227 AU.GIRL. P
ϕ=236.6° Δ= 93.1°
107 AU.GIRL. P
ϕ=236.6° Δ= 93.1°
408 II.KAPI.00 P
ϕ=241.8° Δ= 75.5°
219 II.KAPI.00 P
ϕ=241.8° Δ= 75.5°
279 AU.XMI. P
ϕ=250.3° Δ= 87.9°
136 AU.XMI. P
ϕ=250.3° Δ= 87.9°
327 MY.KOM. P
ϕ=259.1° Δ= 79.3°
182 MY.KOM. P
ϕ=259.1° Δ= 79.3°
358 IC.QIZ.00 P
ϕ=265.8° Δ= 62.3°
149 IC.QIZ.00 P
ϕ=265.8° Δ= 62.3°
243 IU.INCN.00 P
ϕ=269.4° Δ= 38.9°
140 IU.INCN.00 P
ϕ=269.4° Δ= 38.9°
430 IU.CHTO.00 P
ϕ=274.2° Δ= 69.2°
238 IU.CHTO.00 P
ϕ=274.2° Δ= 69.2°
547 IC.BJT.00 P
ϕ=280.1° Δ= 43.8°
316 IC.BJT.00 P
ϕ=280.1° Δ= 43.8°
405 IC.LSA.00 P
ϕ=287.8° Δ= 65.9°
179 IC.LSA.00 P
ϕ=287.8° Δ= 65.9°
266 IU.ULN.00 P
ϕ=294.7° Δ= 44.7°
101 IU.ULN.00 P
ϕ=294.7° Δ= 44.7°
526 II.TLY.00 P
ϕ=301.0° Δ= 44.5°
273 II.TLY.00 P
ϕ=301.0° Δ= 44.5°
270 II.NIL.00 P
ϕ=302.8° Δ= 72.9°
93 II.NIL.00 P
ϕ=302.8° Δ= 72.9°
522 IU.KBL. P
ϕ=306.3° Δ= 74.4°
156 IU.KBL. P
ϕ=306.3° Δ= 74.4°
719 II.AAK.00 P
ϕ=308.2° Δ= 65.4°
209 II.AAK.00 P
ϕ=308.2° Δ= 65.4°
438 II.UOSS.00 P
ϕ=310.1° Δ= 88.6°
123 II.UOSS.00 P
ϕ=310.1° Δ= 88.6°
585 II.BRVK.00 P
ϕ=318.5° Δ= 59.6°
173 II.BRVK.00 P
ϕ=318.5° Δ= 59.6°
444 II.KIV.00 P
ϕ=329.2° Δ= 77.3°
135 II.KIV.00 P
ϕ=329.2° Δ= 77.3°
735 IU.ANTO.00 P
ϕ=334.4° Δ= 84.0°
232 IU.ANTO.00 P
ϕ=334.4° Δ= 84.0°
347 II.OBN.00 P
ϕ=337.9° Δ= 68.9°
85 II.OBN.00 P
ϕ=337.9° Δ= 68.9°
293 MN.VTS. P
ϕ=342.1° Δ= 83.6°
102 MN.VTS. P
ϕ=342.1° Δ= 83.6°
643 IU.KEV.00 P
ϕ=348.7° Δ= 57.0°
182 IU.KEV.00 P
ϕ=348.7° Δ= 57.0°
390 II.BFO.00 P
ϕ=353.6° Δ= 79.9°
154 II.BFO.00 P
ϕ=353.6° Δ= 79.9°
499 G.CLF.00 P
ϕ=357.6° Δ= 80.5°
142 G.CLF.00 P
ϕ=357.6° Δ= 80.5°
644 II.ESK.00 SH
ϕ= 1.2° Δ= 73.2°
207 II.ESK.00 SH
ϕ= 1.2° Δ= 73.2°
875 IU.PAB.00 SH
ϕ= 2.4° Δ= 89.0°
216 IU.PAB.00 SH
ϕ= 2.4° Δ= 89.0°
496 II.BORG.00 SH
ϕ= 9.5° Δ= 62.8°
153 II.BORG.00 SH
ϕ= 9.5° Δ= 62.8°
689 DK.ICESG.00 SH
ϕ= 15.5° Δ= 56.2°
231 DK.ICESG.00 SH
ϕ= 15.5° Δ= 56.2°
413 II.CMLA.00 SH
ϕ= 19.0° Δ= 88.3°
156 II.CMLA.00 SH
ϕ= 19.0° Δ= 88.3°
381 G.IVI.00 SH
ϕ= 23.7° Δ= 61.3°
148 G.IVI.00 SH
ϕ= 23.7° Δ= 61.3°
328 CN.FRB. SH
ϕ= 30.6° Δ= 53.5°
131 CN.FRB. SH
ϕ= 30.6° Δ= 53.5°
289 CN.SCHQ. SH
ϕ= 37.1° Δ= 60.6°
197 CN.SCHQ. SH
ϕ= 37.1° Δ= 60.6°
178 IU.HRV.00 SH
ϕ= 48.5° Δ= 68.1°
81 IU.HRV.00 SH
ϕ= 48.5° Δ= 68.1°
189 CN.SADO. SH
ϕ= 51.5° Δ= 62.8°
96 CN.SADO. SH
ϕ= 51.5° Δ= 62.8°
111 CN.ULM. SH
ϕ= 55.7° Δ= 50.7°
50 CN.ULM. SH
ϕ= 55.7° Δ= 50.7°
178 IU.WCI.00 SH
ϕ= 60.9° Δ= 63.8°
110 IU.WCI.00 SH
ϕ= 60.9° Δ= 63.8°
171 IU.DWPF.00 SH
ϕ= 64.8° Δ= 74.1°
114 IU.DWPF.00 SH
ϕ= 64.8° Δ= 74.1°
240 IU.HKT.00 SH
ϕ= 73.6° Δ= 64.4°
112 IU.HKT.00 SH
ϕ= 73.6° Δ= 64.4°
308 II.JTS.00 SH
ϕ= 78.7° Δ= 85.9°
177 II.JTS.00 SH
ϕ= 78.7° Δ= 85.9°
269 G.UNM.00 SH
ϕ= 83.8° Δ= 70.2°
112 G.UNM.00 SH
ϕ= 83.8° Δ= 70.2°
466 II.PFO.00 SH
ϕ= 85.2° Δ= 49.3°
169 II.PFO.00 SH
ϕ= 85.2° Δ= 49.3°
359 IU.PAYG.00 SH
ϕ= 89.7° Δ= 91.1°
125 IU.PAYG.00 SH
ϕ= 89.7° Δ= 91.1°
437 IU.PTCN.00 SH
ϕ=135.1° Δ= 88.7°
199 IU.PTCN.00 SH
ϕ=135.1° Δ= 88.7°
1099 G.TAOE.00 SH
ϕ=136.3° Δ= 70.0°
204 G.TAOE.00 SH
ϕ=136.3° Δ= 70.0°
995 G.PPTF.00 SH
ϕ=148.7° Δ= 74.4°
144 G.PPTF.00 SH
ϕ=148.7° Δ= 74.4°
963 IU.RAR.00 SH
ϕ=159.4° Δ= 75.1°
195 IU.RAR.00 SH
ϕ=159.4° Δ= 75.1°
745 AU.NIUE. SH
ϕ=168.7° Δ= 71.3°
189 AU.NIUE. SH
ϕ=168.7° Δ= 71.3°
652 IU.AFI.00 SH
ϕ=170.0° Δ= 65.9°
144 IU.AFI.00 SH
ϕ=170.0° Δ= 65.9°
676 IU.FUNA.00 SH
ϕ=179.5° Δ= 60.1°
120 IU.FUNA.00 SH
ϕ=179.5° Δ= 60.1°
619 IU.TARA.00 SH
ϕ=187.6° Δ= 50.5°
166 IU.TARA.00 SH
ϕ=187.6° Δ= 50.5°
838 G.NOUC.00 SH
ϕ=192.0° Δ= 74.4°
178 G.NOUC.00 SH
ϕ=192.0° Δ= 74.4°
640 IU.HNR.00 SH
ϕ=200.9° Δ= 63.1°
97 IU.HNR.00 SH
ϕ=200.9° Δ= 63.1°
1262 IU.CTAO.00 SH
ϕ=211.2° Δ= 77.0°
200 IU.CTAO.00 SH
ϕ=211.2° Δ= 77.0°
886 IU.PMG.00 SH
ϕ=214.2° Δ= 66.8°
114 IU.PMG.00 SH
ϕ=214.2° Δ= 66.8°
1121 IU.GUMO.00 SH
ϕ=228.0° Δ= 46.8°
163 IU.GUMO.00 SH
ϕ=228.0° Δ= 46.8°
1075 II.KAPI.00 SH
ϕ=241.8° Δ= 75.5°
138 II.KAPI.00 SH
ϕ=241.8° Δ= 75.5°
1567 MY.IPM. SH
ϕ=263.1° Δ= 78.9°
243 MY.IPM. SH
ϕ=263.1° Δ= 78.9°
1429 IC.QIZ.00 SH
ϕ=265.8° Δ= 62.3°
217 IC.QIZ.00 SH
ϕ=265.8° Δ= 62.3°
1044 IU.CHTO.00 SH
ϕ=274.2° Δ= 69.2°
232 IU.CHTO.00 SH
ϕ=274.2° Δ= 69.2°
1235 II.PALK.00 SH
ϕ=280.8° Δ= 89.3°
201 II.PALK.00 SH
ϕ=280.8° Δ= 89.3°
1312 IC.LSA.00 SH
ϕ=287.8° Δ= 65.9°
214 IC.LSA.00 SH
ϕ=287.8° Δ= 65.9°
1230 IU.ULN.00 SH
ϕ=294.7° Δ= 44.7°
246 IU.ULN.00 SH
ϕ=294.7° Δ= 44.7°
1399 II.TLY.00 SH
ϕ=301.0° Δ= 44.5°
333 II.TLY.00 SH
ϕ=301.0° Δ= 44.5°
1323 IU.KBL. SH
ϕ=306.3° Δ= 74.4°
360 IU.KBL. SH
ϕ=306.3° Δ= 74.4°
1371 II.UOSS.00 SH
ϕ=310.1° Δ= 88.6°
421 II.UOSS.00 SH
ϕ=310.1° Δ= 88.6°
1326 II.BRVK.00 SH
ϕ=318.5° Δ= 59.6°
396 II.BRVK.00 SH
ϕ=318.5° Δ= 59.6°
1926 II.ARU.00 SH
ϕ=326.9° Δ= 61.4°
262 II.ARU.00 SH
ϕ=326.9° Δ= 61.4°
1494 IU.ANTO.00 SH
ϕ=334.4° Δ= 84.0°
376 IU.ANTO.00 SH
ϕ=334.4° Δ= 84.0°
1401 II.OBN.00 SH
ϕ=337.9° Δ= 68.9°
333 II.OBN.00 SH
ϕ=337.9° Δ= 68.9°
1444 II.LVZ.00 SH
ϕ=344.8° Δ= 57.7°
283 II.LVZ.00 SH
ϕ=344.8° Δ= 57.7°
996 MN.WDD. SH
ϕ=347.3° Δ= 91.7°
203 MN.WDD. SH
ϕ=347.3° Δ= 91.7°
605 G.SSB.00 SH
ϕ=355.9° Δ= 83.2°
100 G.SSB.00 SH
ϕ=355.9° Δ= 83.2°
933 G.CLF.00 SH
ϕ=357.6° Δ= 80.5°
203 G.CLF.00 SH
ϕ=357.6° Δ= 80.5°
1179
128
1719
347
1457
242
1839
309
2541
389
2107
340
2236
323
1992
236
1868
270
2308
417
2448
478
2053
310
1744
381
1717
316
1271
226
1392
177
1269
276
749
289
889
244
0 20 40 60 80 100 120
Time (s)

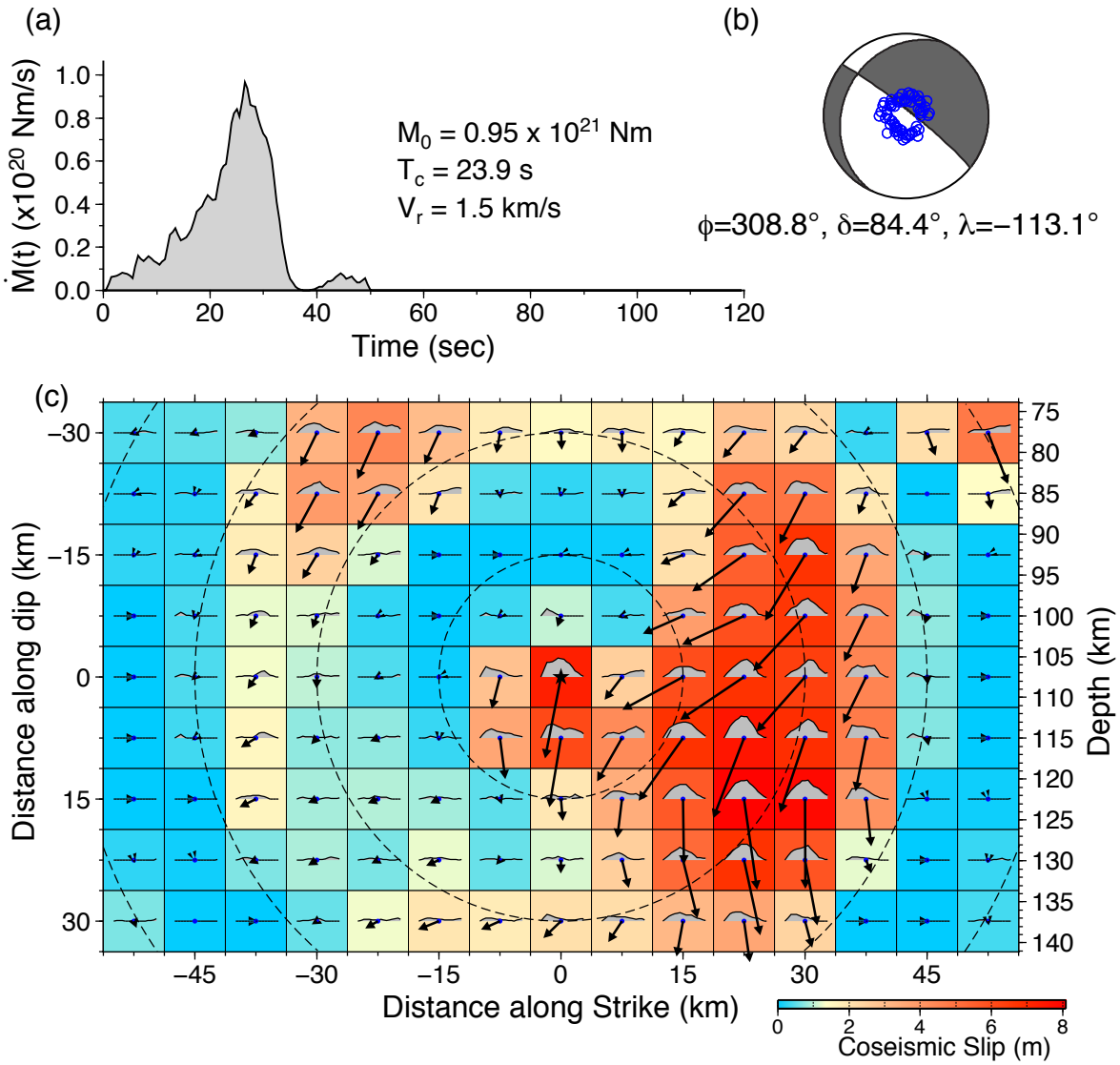
(a)
(b)
$\dot{M}(t)$ (x10^{20} Nm/s)
1.0
0.8
0.6
0.4
0.2
0.0
0
20
40
60
80
100
120
Time (sec)
M_0 = 0.95 x 10^{21} Nm
T_c = 23.9 s
V_r = 1.5 km/s
ϕ=308.8°, δ=84.4°, λ=−113.1°
(c)
Distance along dip (km)
−30
−15
0
15
30
Depth (km)
75
80
85
90
95
100
105
110
115
120
125
130
135
140
−45
−30
−15
0
15
30
45
Distance along Strike (km)
0
2
4
6
8
Coseismic Slip (m)

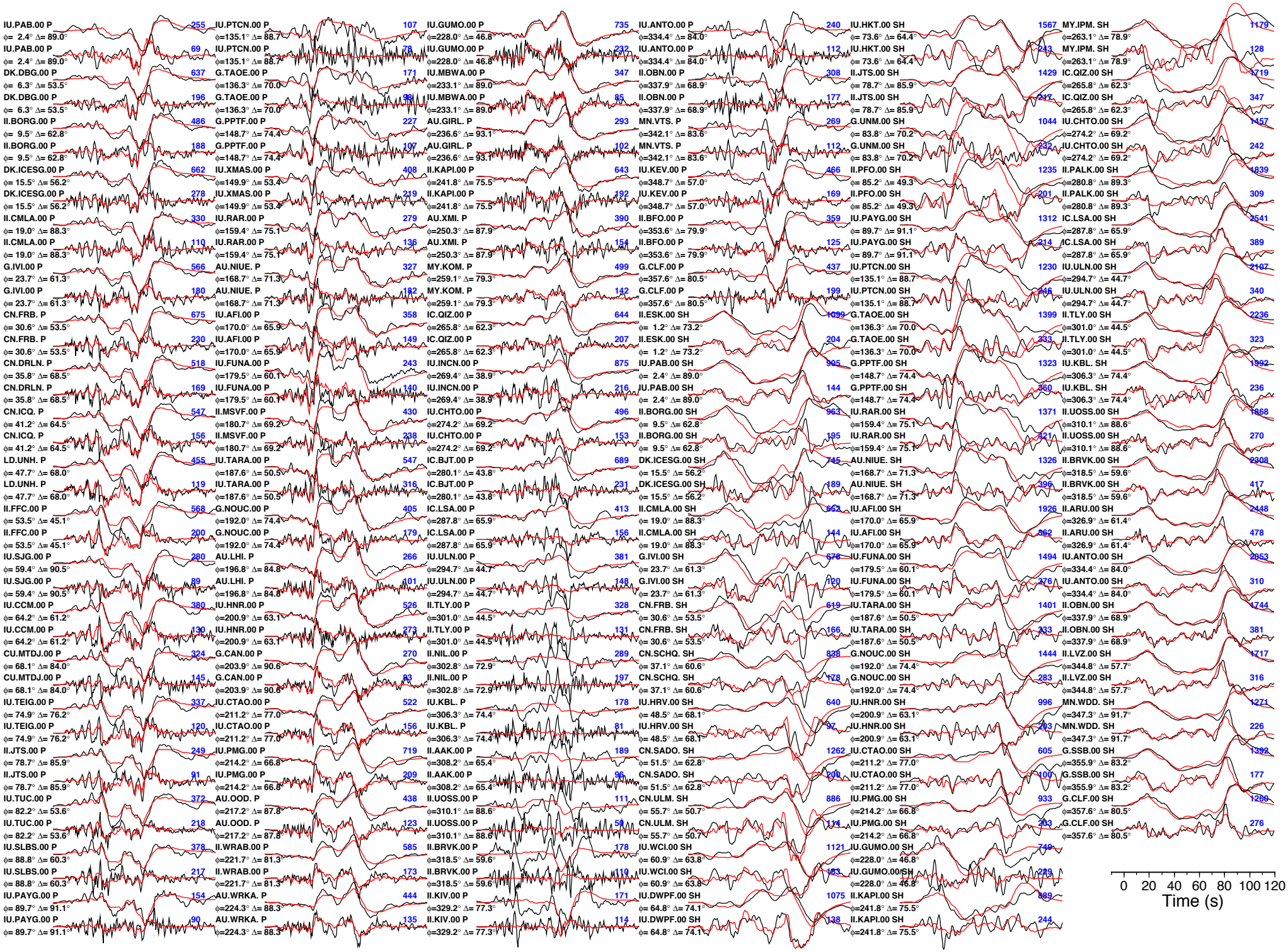
IU.PAB.00 P
ϕ= 2.4° Δ= 89.0°
255 IU.PTCN.00 P
ϕ=135.1° Δ= 88.7°
107 IU.GUMO.00 P
ϕ=228.0° Δ= 46.8°
735 IU.ANTO.00 P
ϕ=334.4° Δ= 84.0°
240 IU.HKT.00 SH
ϕ= 73.6° Δ= 64.4°
1567 MY.IPM. SH
ϕ=263.1° Δ= 78.9°
IU.PAB.00 P
ϕ= 2.4° Δ= 89.0°
69 IU.PTCN.00 P
ϕ=135.1° Δ= 88.7°
78 IU.GUMO.00 P
ϕ=228.0° Δ= 46.8°
232 IU.ANTO.00 P
ϕ=334.4° Δ= 84.0°
112 IU.HKT.00 SH
ϕ= 73.6° Δ= 64.4°
243 MY.IPM. SH
ϕ=263.1° Δ= 78.9°
128
DK.DBG.00 P
ϕ= 6.3° Δ= 53.5°
637 G.TAOE.00 P
ϕ=136.3° Δ= 70.0°
171 IU.MBWA.00 P
ϕ=233.1° Δ= 89.0°
347 II.OBN.00 P
ϕ=337.9° Δ= 68.9°
308 II.JTS.00 SH
ϕ= 78.7° Δ= 85.9°
1429 IC.QIZ.00 SH
ϕ=265.8° Δ= 62.3°
1719
DK.DBG.00 P
ϕ= 6.3° Δ= 53.5°
196 G.TAOE.00 P
ϕ=136.3° Δ= 70.0°
99 IU.MBWA.00 P
ϕ=233.1° Δ= 89.0°
85 II.OBN.00 P
ϕ=337.9° Δ= 68.9°
177 II.JTS.00 SH
ϕ= 78.7° Δ= 85.9°
217 IC.QIZ.00 SH
ϕ=265.8° Δ= 62.3°
347
II.BORG.00 P
ϕ= 9.5° Δ= 62.8°
486 G.PPTF.00 P
ϕ=148.7° Δ= 74.4°
227 AU.GIRL. P
ϕ=236.6° Δ= 93.1°
293 MN.VTS. P
ϕ=342.1° Δ= 83.6°
269 G.UNM.00 SH
ϕ= 83.8° Δ= 70.2°
1044 IU.CHTO.00 SH
ϕ=274.2° Δ= 69.2°
1457
II.BORG.00 P
ϕ= 9.5° Δ= 62.8°
188 G.PPTF.00 P
ϕ=148.7° Δ= 74.4°
107 AU.GIRL. P
ϕ=236.6° Δ= 93.1°
102 MN.VTS. P
ϕ=342.1° Δ= 83.6°
112 G.UNM.00 SH
ϕ= 83.8° Δ= 70.2°
232 IU.CHTO.00 SH
ϕ=274.2° Δ= 69.2°
242
DK.ICESG.00 P
ϕ= 15.5° Δ= 56.2°
662 IU.XMAS.00 P
ϕ=149.9° Δ= 53.4°
408 II.KAPI.00 P
ϕ=241.8° Δ= 75.5°
643 IU.KEV.00 P
ϕ=348.7° Δ= 57.0°
466 II.PFO.00 SH
ϕ= 85.2° Δ= 49.3°
1235 II.PALK.00 SH
ϕ=280.8° Δ= 89.3°
1839
DK.ICESG.00 P
ϕ= 15.5° Δ= 56.2°
278 IU.XMAS.00 P
ϕ=149.9° Δ= 53.4°
219 II.KAPI.00 P
ϕ=241.8° Δ= 75.5°
192 IU.KEV.00 P
ϕ=348.7° Δ= 57.0°
169 II.PFO.00 SH
ϕ= 85.2° Δ= 49.3°
201 II.PALK.00 SH
ϕ=280.8° Δ= 89.3°
309
II.CMLA.00 P
ϕ= 19.0° Δ= 88.3°
330 IU.RAR.00 P
ϕ=159.4° Δ= 75.1°
279 AU.XMI. P
ϕ=250.3° Δ= 87.9°
390 II.BFO.00 P
ϕ=353.6° Δ= 79.9°
359 IU.PAYG.00 SH
ϕ= 89.7° Δ= 91.1°
1312 IC.LSA.00 SH
ϕ=287.8° Δ= 65.9°
2541
II.CMLA.00 P
ϕ= 19.0° Δ= 88.3°
110 IU.RAR.00 P
ϕ=159.4° Δ= 75.1°
136 AU.XMI. P
ϕ=250.3° Δ= 87.9°
154 II.BFO.00 P
ϕ=353.6° Δ= 79.9°
125 IU.PAYG.00 SH
ϕ= 89.7° Δ= 91.1°
214 IC.LSA.00 SH
ϕ=287.8° Δ= 65.9°
389
G.IVI.00 P
ϕ= 23.7° Δ= 61.3°
566 AU.NIUE. P
ϕ=168.7° Δ= 71.3°
327 MY.KOM. P
ϕ=259.1° Δ= 79.3°
499 G.CLF.00 P
ϕ=357.6° Δ= 80.5°
437 IU.PTCN.00 SH
ϕ=135.1° Δ= 88.7°
1230 IU.ULN.00 SH
ϕ=294.7° Δ= 44.7°
2107
G.IVI.00 P
ϕ= 23.7° Δ= 61.3°
180 AU.NIUE. P
ϕ=168.7° Δ= 71.3°
182 MY.KOM. P
ϕ=259.1° Δ= 79.3°
142 G.CLF.00 P
ϕ=357.6° Δ= 80.5°
199 IU.PTCN.00 SH
ϕ=135.1° Δ= 88.7°
246 IU.ULN.00 SH
ϕ=294.7° Δ= 44.7°
340
CN.FRB. P
ϕ= 30.6° Δ= 53.5°
675 IU.AFI.00 P
ϕ=170.0° Δ= 65.9°
358 IC.QIZ.00 P
ϕ=265.8° Δ= 62.3°
644 II.ESK.00 SH
ϕ= 1.2° Δ= 73.2°
1099 G.TAOE.00 SH
ϕ=136.3° Δ= 70.0°
1399 II.TLY.00 SH
ϕ=301.0° Δ= 44.5°
2236
CN.FRB. P
ϕ= 30.6° Δ= 53.5°
230 IU.AFI.00 P
ϕ=170.0° Δ= 65.9°
149 IC.QIZ.00 P
ϕ=265.8° Δ= 62.3°
207 II.ESK.00 SH
ϕ= 1.2° Δ= 73.2°
204 G.TAOE.00 SH
ϕ=136.3° Δ= 70.0°
333 II.TLY.00 SH
ϕ=301.0° Δ= 44.5°
323
CN.DRLN. P
ϕ= 35.8° Δ= 68.5°
518 IU.FUNA.00 P
ϕ=179.5° Δ= 60.1°
243 IU.INCN.00 P
ϕ=269.4° Δ= 38.9°
875 IU.PAB.00 SH
ϕ= 2.4° Δ= 89.0°
905 G.PPTF.00 SH
ϕ=148.7° Δ= 74.4°
1323 IU.KBL. SH
ϕ=306.3° Δ= 74.4°
1992
CN.DRLN. P
ϕ= 35.8° Δ= 68.5°
169 IU.FUNA.00 P
ϕ=179.5° Δ= 60.1°
140 IU.INCN.00 P
ϕ=269.4° Δ= 38.9°
216 IU.PAB.00 SH
ϕ= 2.4° Δ= 89.0°
144 G.PPTF.00 SH
ϕ=148.7° Δ= 74.4°
360 IU.KBL. SH
ϕ=306.3° Δ= 74.4°
236
CN.ICQ. P
ϕ= 41.2° Δ= 64.5°
547 II.MSVF.00 P
ϕ=180.7° Δ= 69.2°
430 IU.CHTO.00 P
ϕ=274.2° Δ= 69.2°
496 II.BORG.00 SH
ϕ= 9.5° Δ= 62.8°
963 IU.RAR.00 SH
ϕ=159.4° Δ= 75.1°
1371 II.UOSS.00 SH
ϕ=310.1° Δ= 88.6°
1868
CN.ICQ. P
ϕ= 41.2° Δ= 64.5°
156 II.MSVF.00 P
ϕ=180.7° Δ= 69.2°
238 IU.CHTO.00 P
ϕ=274.2° Δ= 69.2°
153 II.BORG.00 SH
ϕ= 9.5° Δ= 62.8°
195 IU.RAR.00 SH
ϕ=159.4° Δ= 75.1°
421 II.UOSS.00 SH
ϕ=310.1° Δ= 88.6°
270
LD.UNH. P
ϕ= 47.7° Δ= 68.0°
455 IU.TARA.00 P
ϕ=187.6° Δ= 50.5°
547 IC.BJT.00 P
ϕ=280.1° Δ= 43.8°
689 DK.ICESG.00 SH
ϕ= 15.5° Δ= 56.2°
745 AU.NIUE. SH
ϕ=168.7° Δ= 71.3°
1326 II.BRVK.00 SH
ϕ=318.5° Δ= 59.6°
2308
LD.UNH. P
ϕ= 47.7° Δ= 68.0°
119 IU.TARA.00 P
ϕ=187.6° Δ= 50.5°
316 IC.BJT.00 P
ϕ=280.1° Δ= 43.8°
231 DK.ICESG.00 SH
ϕ= 15.5° Δ= 56.2°
189 AU.NIUE. SH
ϕ=168.7° Δ= 71.3°
396 II.BRVK.00 SH
ϕ=318.5° Δ= 59.6°
417
II.FFC.00 P
ϕ= 53.5° Δ= 45.1°
568 G.NOUC.00 P
ϕ=192.0° Δ= 74.4°
405 IC.LSA.00 P
ϕ=287.8° Δ= 65.9°
413 II.CMLA.00 SH
ϕ= 19.0° Δ= 88.3°
662 IU.AFI.00 SH
ϕ=170.0° Δ= 65.9°
1926 II.ARU.00 SH
ϕ=326.9° Δ= 61.4°
2448
II.FFC.00 P
ϕ= 53.5° Δ= 45.1°
200 G.NOUC.00 P
ϕ=192.0° Δ= 74.4°
179 IC.LSA.00 P
ϕ=287.8° Δ= 65.9°
156 II.CMLA.00 SH
ϕ= 19.0° Δ= 88.3°
144 IU.AFI.00 SH
ϕ=170.0° Δ= 65.9°
562 II.ARU.00 SH
ϕ=326.9° Δ= 61.4°
478
IU.SJG.00 P
ϕ= 59.4° Δ= 90.5°
280 AU.LHI. P
ϕ=196.8° Δ= 84.8°
266 IU.ULN.00 P
ϕ=294.7° Δ= 44.7°
381 G.IVI.00 SH
ϕ= 23.7° Δ= 61.3°
678 IU.FUNA.00 SH
ϕ=179.5° Δ= 60.1°
1494 IU.ANTO.00 SH
ϕ=334.4° Δ= 84.0°
2853
IU.SJG.00 P
ϕ= 59.4° Δ= 90.5°
89 AU.LHI. P
ϕ=196.8° Δ= 84.8°
101 IU.ULN.00 P
ϕ=294.7° Δ= 44.7°
148 G.IVI.00 SH
ϕ= 23.7° Δ= 61.3°
120 IU.FUNA.00 SH
ϕ=179.5° Δ= 60.1°
376 IU.ANTO.00 SH
ϕ=334.4° Δ= 84.0°
310
IU.CCM.00 P
ϕ= 64.2° Δ= 61.2°
380 IU.HNR.00 P
ϕ=200.9° Δ= 63.1°
526 II.TLY.00 P
ϕ=301.0° Δ= 44.5°
328 CN.FRB. SH
ϕ= 30.6° Δ= 53.5°
619 IU.TARA.00 SH
ϕ=187.6° Δ= 50.5°
1401 II.OBN.00 SH
ϕ=337.9° Δ= 68.9°
1744
IU.CCM.00 P
ϕ= 64.2° Δ= 61.2°
130 IU.HNR.00 P
ϕ=200.9° Δ= 63.1°
273 II.TLY.00 P
ϕ=301.0° Δ= 44.5°
131 CN.FRB. SH
ϕ= 30.6° Δ= 53.5°
166 IU.TARA.00 SH
ϕ=187.6° Δ= 50.5°
433 II.OBN.00 SH
ϕ=337.9° Δ= 68.9°
381
CU.MTDJ.00 P
ϕ= 68.1° Δ= 84.0°
324 G.CAN.00 P
ϕ=203.9° Δ= 90.6°
270 II.NIL.00 P
ϕ=302.8° Δ= 72.9°
289 CN.SCHQ. SH
ϕ= 37.1° Δ= 60.6°
838 G.NOUC.00 SH
ϕ=192.0° Δ= 74.4°
1444 II.LVZ.00 SH
ϕ=344.8° Δ= 57.7°
1717
CU.MTDJ.00 P
ϕ= 68.1° Δ= 84.0°
145 G.CAN.00 P
ϕ=203.9° Δ= 90.6°
83 II.NIL.00 P
ϕ=302.8° Δ= 72.9°
197 CN.SCHQ. SH
ϕ= 37.1° Δ= 60.6°
178 G.NOUC.00 SH
ϕ=192.0° Δ= 74.4°
283 II.LVZ.00 SH
ϕ=344.8° Δ= 57.7°
316
IU.TEIG.00 P
ϕ= 74.9° Δ= 76.2°
337 IU.CTAO.00 P
ϕ=211.2° Δ= 77.0°
522 IU.KBL. P
ϕ=306.3° Δ= 74.4°
178 IU.HRV.00 SH
ϕ= 48.5° Δ= 68.1°
640 IU.HNR.00 SH
ϕ=200.9° Δ= 63.1°
996 MN.WDD. SH
ϕ=347.3° Δ= 91.7°
1271
IU.TEIG.00 P
ϕ= 74.9° Δ= 76.2°
120 IU.CTAO.00 P
ϕ=211.2° Δ= 77.0°
156 IU.KBL. P
ϕ=306.3° Δ= 74.4°
81 IU.HRV.00 SH
ϕ= 48.5° Δ= 68.1°
97 IU.HNR.00 SH
ϕ=200.9° Δ= 63.1°
203 MN.WDD. SH
ϕ=347.3° Δ= 91.7°
226
II.JTS.00 P
ϕ= 78.7° Δ= 85.9°
249 IU.PMG.00 P
ϕ=214.2° Δ= 66.8°
719 II.AAK.00 P
ϕ=308.2° Δ= 65.4°
189 CN.SADO. SH
ϕ= 51.5° Δ= 62.8°
1262 IU.CTAO.00 SH
ϕ=211.2° Δ= 77.0°
605 G.SSB.00 SH
ϕ=355.9° Δ= 83.2°
1392
II.JTS.00 P
ϕ= 78.7° Δ= 85.9°
91 IU.PMG.00 P
ϕ=214.2° Δ= 66.8°
209 II.AAK.00 P
ϕ=308.2° Δ= 65.4°
96 CN.SADO. SH
ϕ= 51.5° Δ= 62.8°
200 IU.CTAO.00 SH
ϕ=211.2° Δ= 77.0°
100 G.SSB.00 SH
ϕ=355.9° Δ= 83.2°
177
IU.TUC.00 P
ϕ= 82.2° Δ= 53.6°
372 AU.OOD. P
ϕ=217.2° Δ= 87.8°
438 II.UOSS.00 P
ϕ=310.1° Δ= 88.6°
111 CN.ULM. SH
ϕ= 55.7° Δ= 50.7°
886 IU.PMG.00 SH
ϕ=214.2° Δ= 66.8°
933 G.CLF.00 SH
ϕ=357.6° Δ= 80.5°
1280
IU.TUC.00 P
ϕ= 82.2° Δ= 53.6°
218 AU.OOD. P
ϕ=217.2° Δ= 87.8°
123 II.UOSS.00 P
ϕ=310.1° Δ= 88.6°
50 CN.ULM. SH
ϕ= 55.7° Δ= 50.7°
114 IU.PMG.00 SH
ϕ=214.2° Δ= 66.8°
203 G.CLF.00 SH
ϕ=357.6° Δ= 80.5°
276
IU.SLBS.00 P
ϕ= 88.8° Δ= 60.3°
378 II.WRAB.00 P
ϕ=221.7° Δ= 81.3°
585 II.BRVK.00 P
ϕ=318.5° Δ= 59.6°
178 IU.WCI.00 SH
ϕ= 60.9° Δ= 63.8°
1121 IU.GUMO.00 SH
ϕ=228.0° Δ= 46.8°
749
IU.SLBS.00 P
ϕ= 88.8° Δ= 60.3°
217 II.WRAB.00 P
ϕ=221.7° Δ= 81.3°
173 II.BRVK.00 P
ϕ=318.5° Δ= 59.6°
110 IU.WCI.00 SH
ϕ= 60.9° Δ= 63.8°
153 IU.GUMO.00 SH
ϕ=228.0° Δ= 46.8°
289
IU.PAYG.00 P
ϕ= 89.7° Δ= 91.1°
154 AU.WRKA. P
ϕ=224.3° Δ= 88.3°
444 II.KIV.00 P
ϕ=329.2° Δ= 77.3°
171 IU.DWPF.00 SH
ϕ= 64.8° Δ= 74.1°
1075 II.KAPI.00 SH
ϕ=241.8° Δ= 75.5°
889
IU.PAYG.00 P
ϕ= 89.7° Δ= 91.1°
90 AU.WRKA. P
ϕ=224.3° Δ= 88.3°
135 II.KIV.00 P
ϕ=329.2° Δ= 77.3°
114 IU.DWPF.00 SH
ϕ= 64.8° Δ= 74.1°
138 II.KAPI.00 SH
ϕ=241.8° Δ= 75.5°
244
0 20 40 60 80 100 120
Time (s)

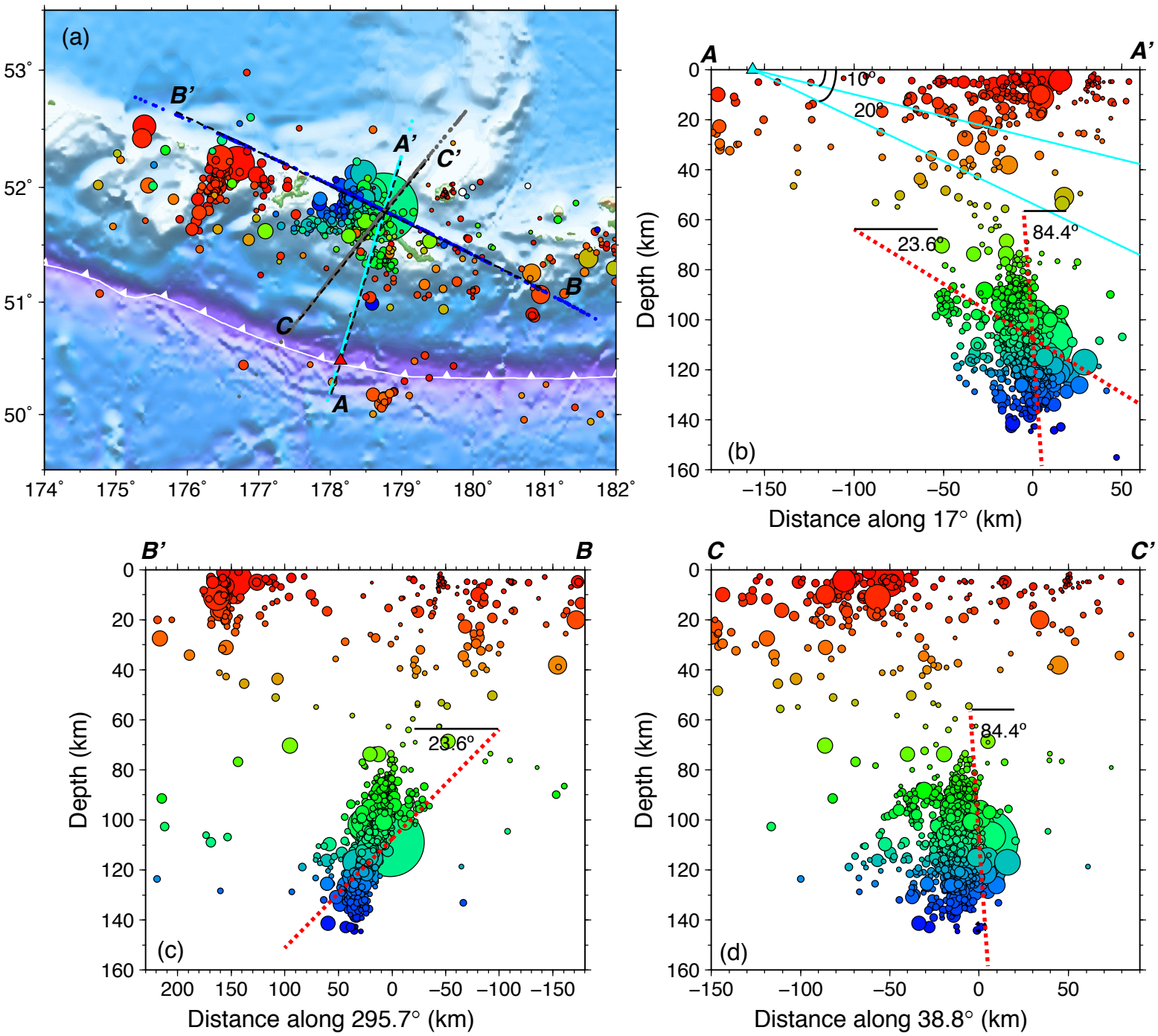
(a)
B'
A'
C'
B
C
A
53°
52°
51°
50°
174°
175°
176°
177°
178°
179°
180°
181°
182°
A
A'
10°
20°
23.6°
84.4°
Depth (km)
(b)
Distance along 17° (km)
B'
B
23.6°
(c)
Distance along 295.7° (km)
C
C'
84.4°
(d)
Distance along 38.8° (km)

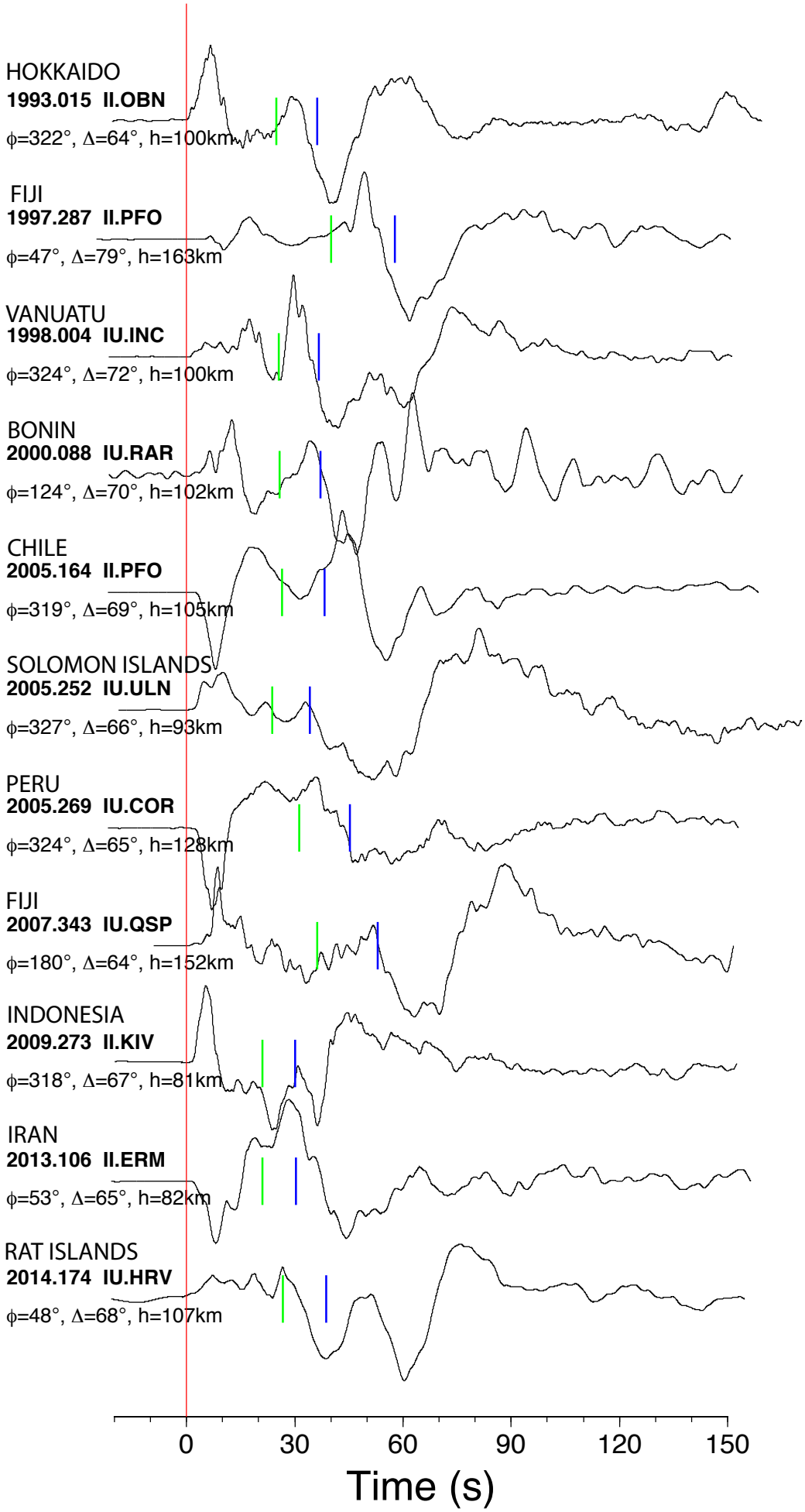
HOKKAIDO
1993.015 II.OBN
ϕ=322°, Δ=64°, h=100km
FIJI
1997.287 II.PFO
ϕ=47°, Δ=79°, h=163km
VANUATU
1998.004 IU.INC
ϕ=324°, Δ=72°, h=100km
BONIN
2000.088 IU.RAR
ϕ=124°, Δ=70°, h=102km
CHILE
2005.164 II.PFO
ϕ=319°, Δ=69°, h=105km
SOLOMON ISLANDS
2005.252 IU.ULN
ϕ=327°, Δ=66°, h=93km
PERU
2005.269 IU.COR
ϕ=324°, Δ=65°, h=128km
FIJI
2007.343 IU.QSP
ϕ=180°, Δ=64°, h=152km
INDONESIA
2009.273 II.KIV
ϕ=318°, Δ=67°, h=81km
IRAN
2013.106 II.ERM
ϕ=53°, Δ=65°, h=82km
RAT ISLANDS
2014.174 IU.HRV
ϕ=48°, Δ=68°, h=107km
0
30
60
90
120
150
Time (s)